Scaling laws in directional spreading of droplets on wettability-confined diverging tracks

Uddalok Sen,[†] Souvick Chatterjee,[†] Ranjan Ganguly,[‡] Richard Dodge,[¶] Lisha Yu,[¶] and Constantine M. Megaridis[*,†]

[†]*Department of Mechanical and Industrial Engineering, University of Illinois at Chicago, Chicago, IL 60607, USA*

[‡]*Department of Power Engineering, Jadavpur University, Kolkata 700098, India*

[¶]*Corporate Research and Engineering, Kimberly-Clark Corporation, Neenah, WI 54956, USA*

E-mail: cmm@uic.edu

Abstract

Spontaneous pumpless transport of droplets on wettability-confined tracks is important for various applications, such as rapid transport and mixing of fluid droplets, enhanced dropwise condensation, biomedical devices, etc. Recent studies have shown that on an open surface, a superhydrophilic track of diverging width, laid on a superhydrophobic background, facilitates the transport of water from the narrower end to the wider end at unprecedented rates (up to 40 cm/s), without external actuation. The spreading behavior on such surfaces, however, has only been characterized for water. Keeping in mind that such designs play a key role for a diverse range of applications handling organic liquids and in point-of-care devices, the importance of characterizing the spreading behavior of viscous liquids on such surfaces cannot be overemphasized. In the present work, the spreading behavior on the aforementioned wettability-patterned diverging tracks was observed for fluids of different viscosities. Two dimensionless variables were identified, and a comprehensive relationship was obtained. Three distinct temporal scales of droplet spreading were established: first, a Washburn-type slow spreading, followed by a much faster Laplace-pressure driven spreading, and finally, a sluggish density augmented-Tanner-type film spreading. The results offer design guidance for tracks that can pumplessly manage fluids of various viscosities and surface tensions.

Introduction

Open-surface microfluidics, a subgenre that deals with liquid microvolumes on open surfaces, has recently developed into an important strategy for performing various microdroplet handling tasks.[1] Such devices are essentially of two-dimensional nature, and can be fabricated in a timespan that is, in most cases, an order of magnitude shorter than the times required for conventional three-dimensional closed channel microfluidic systems, which typically are fabricated using complex and costly fabrication procedures. Moreover, closed-channel microfluidic systems are associated with several practical difficulties, such as channel clogging by bubbles[2] and fouling by debris.[3] Non-specific interactions of the analyte/reagent with the walls of the channel also cannot be avoided in some cases, which leads to false analysis outcomes. These issues are non-existent in open-channel microfluidic systems, where the liquid need not be confined by solid channel walls. This allows for a diverse range of substrates, such as rigid

and flexible solids,[4] porous materials,[5] and even liquid-infused hybrid materials.[6]

Open-surface or open-channel microfluidics are, in essence, a category of digital microfluidics,[7] where individual fluid droplets, instead of a continuous fluid volume, are handled as the analyte. Actuation of droplets on such devices can be achieved by several methods, such as electrowetting on dielectric (EWOD),[8] optoelectrowetting (OEW),[9] magnetic,[10] and acoustic[11] approaches, among others. Since the characteristic length scale of the droplet in such devices is almost always below the capillary length,[12] forces due to the liquid surface tension, arising from spatial changes in the surface energy of the substrate or the droplet itself, can be harnessed for manipulating the liquid volume. The surface energy barrier at the contrast line between superhydrophobic and superhydrophilic domains can be utilized to confine droplets of water,[13] with the maximum liquid handling capacity being dictated by the sessile-droplet contact angles at the two domains.[14] The recent proliferation of facile techniques to create surfaces[15] with extreme wettability contrast has led to the development of technologies[16–20] that can handle liquid droplets on the surface of a chip or a substrate using the so-called surface tension confinement, where a liquid volume is confined on a wettable region bounded by a repellent domain. Such techniques of wettability patterning have also been used in applications as diverse as atmospheric water collection[21] and surface-enhanced Raman spectroscopy (SERS).[22–24] It is important to note that strategies for handling liquids could be extended to porous substrates, such as paper[25] and fabrics as well.[26]

Droplet transport on surface tension-confined tracks requires a source of actuation, such as gravity[19] or a difference in the Laplace pressure of two droplets (of different diameters) connected by a track.[20] However, 'pumpless' actuation of droplets on surface-tension-confined tracks can be achieved if one is able to change the surface energy of the liquid in a dynamic fashion.[27] A droplet on a substrate will always seek to minimize the overall energy of the system, which can be used to achieve spontaneous, directional movement of the droplet on a suitably-designed substrate. Physical texturing or micropatterning of the substrate is a popular technique in this regard,[28–30] where the roughness of the substrate varies in space, which leads to a spatial nonuniformity in the affinity of the droplet towards the substrate. Other techniques of pumpless transport include creation of a surface energy gradient by chemical modification of the substrate[31] or the droplet,[32,33] differential heating of the substrate in the presence of a hydrophilicity gradient,[34] photo irradiation,[35] and chemically-assisted thermocapillary migration,[36] among others. The various methods of creating wettability gradients by way of external fields have been extensively reviewed by Li et al.[37]

Recently, Ghosh et al.[4] introduced a liquid manipulation technique where a water droplet was observed to undergo self-propulsion from the narrower end to the wider end of a diverging or wedge-shaped superhydrophilic track laid on a superhydrophobic substrate. The constantly changing droplet footprint area on such a track, and the resulting axial variation of the curvature of the liquid meniscus led to a net Laplace pressure-generated force along the axial direction of the track, which drove the droplet. Such a configuration can also be used for tranporting water droplets up an incline against gravity.[4,38,39] The geometry of this particular design resembles a two-dimensional analog of spontaneous, unidirectional droplet spreading on a conical wire.[40] Khoo and Tseng[41] used the same configuration for pumpless transport of subnanoliter droplets, while Alheshibri et al.[42] leveraged the difference in contact angles of water on copper and aluminium to create planar domains possessing contrasting wettability in order to drive a droplet. The usefulness and versatility of the wettability-confined diverging track is evident from the diverse array of applications in which such a design has been employed. Nakajima et al.[43] used several such triangular patches for liquid manipulation, while Morrissette et al.[44] used the design for spontaneous transport, mixing, and reaction of two aqueous droplets containing different reagents. Wettability patterns with the superhydrophilic

wedge tracks as key functional element have also been shown to enhance the heat transfer performance in dropwise condensation studies[45–47] and for electronics cooling.[48]

Use of wettability-confined tracks is not limited to transporting water only; recent studies have shown that such a configuration can be also used for transporting droplets of organic liquids under water[49] and ferrofluids[50] as well. When transporting different liquids on the wedge-shaped tracks, two fluid properties play crucial roles – surface tension and viscosity. The effect of surface tension is apparent, since it is responsible for the Laplace pressure driving the fluid. The extent of the role of viscosity, however, cannot be inferred right away, as it would warrant *a priori* knowledge of the transport dynamics on the wedge track. This calls for a rigorous experimental investigation of the effect of viscosity on the pumping ability of such wedge-shaped tracks. Moreover, since a major application area of microfluidics is the healthcare industry (point-of-care devices), where the liquid being transported is a complex fluid, studying fluids other than water is of utmost importance. Although a vast pool of literature exists on dynamic spreading of liquids on homogeneous surfaces,[51–54] no such work exists on the spreading dynamics on wedge-shaped wettability-confined tracks. Hence, an attempt to understand the same in pumpless transport of aqueous liquids on wettability-confined diverging tracks through a parametric variation of the liquid viscosity is made in the present work. The transport characteristics are studied with aqueous solutions of glycerol having different mass fractions, hence different viscosities. A common behavior of such droplets is revealed, where the spreading front follows three distinct and successive temporal scaling laws.

Materials and Methods

A facile and scalable approach towards producing superhydrophobic and superhydrophilic domains on rectangular aluminum samples of dimensions 25 mm × 50 mm (mirror-finish 6061 aluminum sheets, 2 mm thick, McMaster-Carr), was followed in the present work. The method is identical to the one employed by Koukoravas et al.,[48] and is shown schematically in Fig. 1. The samples were initially treated with a 4 M HCl solution (ACS Reagent 37%, Sigma-Aldrich) for 5 minutes (Fig. 1a) and then passivated in boiling deionized water for 60 minutes (Fig. 1c). This facilitated the growth of micro-nano structures on the surface of the sample. The boiling step resulted in the formation of a thin layer of aluminum oxide hydroxide (Al(O)OH) or böhmite on the surface of the substrate,[55] resulting in superhydrophilic behavior (water contact angles $\sim 0^\circ$). As done by previous researchers,[56,57] the superhydrophilic aluminum samples were then immersed in a 1% (by weight) solution of 1H, 1H, 2H, 2H - Perfluorodecyltriethoxysilane (97%, Sigma-Aldrich, abbreviated as FAS for fluoro-alkyl silane) in ethanol (200 proof, Decon Labs) for 8 - 10 hours (Fig. 1e). This step resulted in the deposition of a monolayer of FAS on the roughened Al substrates, thus imparting superhydrophobicity to the surface. Scanning electron micrographs (obtained using the imaging module of a Raith 100 eLINE Electron Beam Lithography System) at different stages of sample preparation are shown in Figs. 1b and 1d. Microscale terraces and caverns are formed after acid-etching (Fig. 1b), which are subsequently covered by nanoscale böhmite needles (Fig. 1e) upon passivation in boiling water. Such surface roughness features with nanoscale structures formed on top (hierarchical structure) are critical for achieving either superhydrophilic or superhydrophobic behavior. The average roughness of the surfaces was found to be ~ 25 μm (measured using a Wyko NT3300 Optical Profilometer). The surface energy of the exposed area of the sample is reduced when covered with a monolayer of FAS. A computer-aided design (CAD) file was fed as a vector image to a laser marking system (EMS400, TYKMA Electrox), and the FAS coating on the Al samples was ablated using a Yb laser (20% power, 20 kHz frequency, 200 mm/s traverse speed, Scorpion Rapide, TYKMA Electrox)(Fig. 1f). The laser ablation exposed the underlying superhydrophilic structure, while the unablated regions

retained their superhydrophobic property. Expectedly, a scanning electron micrograph of the laser-ablated region (Fig. S1 of the Supplementary Information) looks similar to that of the superhydrophilic region (Fig. 1d). The sessile water droplet contact angles on the superhydrophobic domains, as measured by an in-house goniometer, was found to be $152 \pm 5^\circ$ (Fig. 1h); a droplet deposited on the superhydrophilic domain spread instantly with a contact angle below 5°. A schematic top view of the finished sample obtained from the above procedure is shown in Fig. 1g, along with its salient dimensions. In the present work, a track of length (L) 30 mm, narrow end width (δ_0) of 500 μm, and divergence angle (α) of 4° was chosen for all tests.

Solutions of glycerol (99+%, Alfa Aesar) of different mass fractions in deioinized water, varying from 0.1 – 0.5 in steps of 0.1, were used as working fluids. A schematic of the experimental setup is shown in Fig. 2. A single drop ($\sim$ 4.5 mg) was dispensed onto the superhydrophilic tracks using a syringe infusion pump (PHD Ultra, Harvard Apparatus) through a 100 μm inner diameter needle (32GA GP, Nordson EFD). The needle distance from the substrate was adjusted so that the droplet detached from the needle just before its bottom touched the track. This assured that the droplet was dispensed at the desired location of the substrate with negligible inertial effects. The fluid flow on the superhydrophilic tracks was imaged at 1000 fps using a high-speed camera (Phantom Miro 310, Vision Research AMETEK with Nikkor 50 mm, Nikon lens). A portable halogen light source (L860, 250 W, Workforce) was used to illuminate the sample through a rectangular diffuser sheet (Lumen XT LT LW7, Makrolon). Sequential time-lapsed images obtained from the high-speed camera were analyzed using the image processing feature of MATLAB, where the instantaneous position of the liquid front was identified by a sharp jump in pixel intensity.

Results and Discussion

Water and aqueous solutions of glycerol (having glycerol mass fraction, C_m, ranging from 0.1 – 0.5) were used as working fluids. In each case, a droplet of $\sim$ 4.5 mg was deposited at the narrower end of a wedge-shaped track of length 30 mm, initial width 500 μm, and divergence angle of 4°. All the experiments were performed at an ambient temperature of 25° C, and the salient properties of the fluids at that condition are presented in Table 1.

Liquid spreading

Time-lapse images of different stages of spreading of a water droplet on the wedge-shaped track are shown in Fig. 3. The nearly-spherical water droplet is dispensed on the narrow end (left) of the track without any initial velocity (Fig. 3a). The droplet is confined on two sides by the wettability-contrast line, and can only spread in the lengthwise direction toward the wider end of the track (right). Initially, the bulk of the liquid volume remains stationary in the form of a bulge, while a liquid front in the form of a film advances along the track (as marked in Fig. 3b). The bulge remains stationary due to its high inertia, while the liquid film advances as a hemiwicking front[60] through the textured superhydrophilic domain. After some time, the liquid bulge starts to move (Fig. 3c), gradually decreasing in height (Fig. 3d), and soon catches up with the advancing liquid front (Fig. 3e). Subsequently, the liquid bulge disappears and the entire liquid volume spreads as a rivulet (Fig. 3f). The contact angle subtended by the liquid volume along the wettability contrast line on the two sides is not the Young's angle;[12] instead it lies between the respective sessile droplet contact angles on the superhydrophobic and superhydrophilic domains, and gradually decreases as the droplet spreads. As the liquid starts spreading, a cross-section of the liquid film at the section A-A$'$ of Fig. 4a1 will initially look like Fig. 4a2; it will gradually transition to the Fig. 4b2 shape as the liquid front progresses along the track. Brinkmann and Lipowsky[61] pointed out, albeit for rectan-

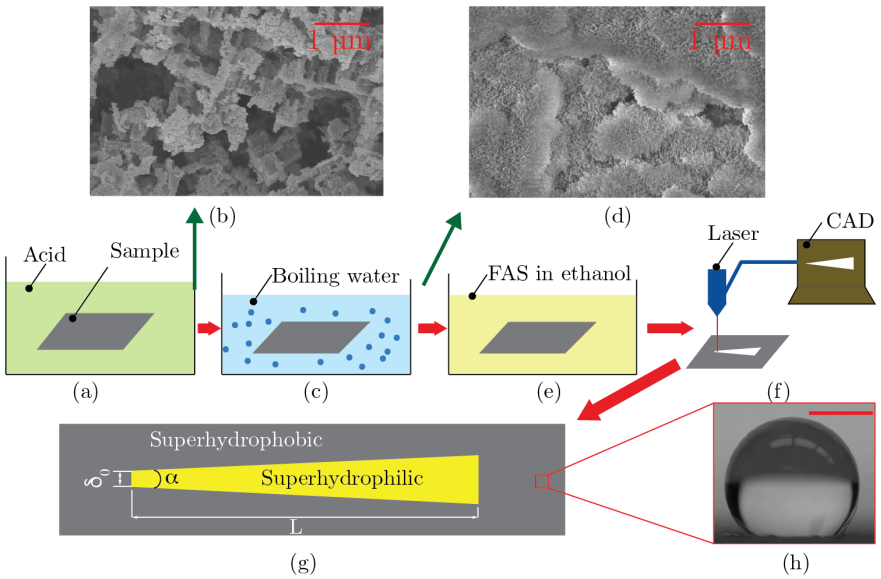

Figure 1: Schematic of the sample preparation procedure: (a) Al samples were treated with 4 M HCl solution for 5 minutes; (b) scanning electron micrograph of acid-etched sample; (c) acid-etched samples were passivated in boiling deionized water for 60 minutes; (d) scanning electron micrograph of etched-and-boiled sample; (e) the etched-and-boiled samples were then treated in an ethanolic solution of fluoro-alkyl silane (FAS) and kept undisturbed for 8 - 10 hours; (f) a CAD-based design was patterned onto the substrate by laser ablation; (g) top view of final sample containing the superhydrophobic and the superhydrophilic domains; (h) sessile water droplet on superhydrophobic domain (scale bar denotes 1 mm)

Table 1: Properties of the different working fluids used in the present work (at 25° C)[58,59]

Glycerol mass fraction, C_m	Density (kg/m^3)	Surface Tension (mN/m)	Viscosity (mPa.s)
0 (water)	997.0	72.45	0.903
0.1	1021.3	71.83	0.928
0.2	1045.5	71.20	1.555
0.3	1072.3	70.28	2.185
0.4	1099.0	69.35	3.220
0.5	1125.3	68.63	5.105

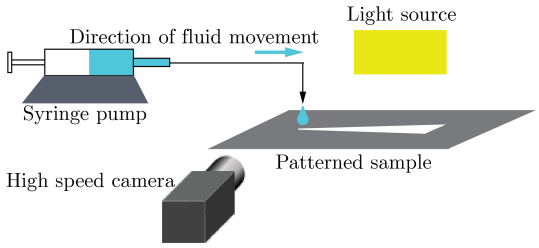

Figure 2: Schematic of the experimental setup

gular channels, that a spreading droplet will form a liquid bulge (which is confined in the transverse and elongated in the axial directions) when the local contact angle along the wettability contrast line exceeds 90°; the morphology is reversible, meaning that the bulge will disappear when the same contact angle becomes less than 90°. The argument can be extended to these diverging tracks – the liquid does form a moving bulge in the initial phase of spreading – although whether the critical local contact angle is still 90° requires detailed theoretical analysis – which is beyond the scope of the present work. The spreading of the liquid droplet essentially occurs as the fluid volume inherently tries to minimize its surface energy. The spreading liquid bulge has a longer contact line on its leading edge as compared to its trailing edge (leading and trailing edges marked as LE and TE, respectively in Fig. 3d). This leads to an unbalanced capillary force (marked as F_{cap} in Figs. 3c and 3d) that drives the liquid volume from the narrow end to the wide end of the track. This capillary force is in the forward direction, as long as the local contact angle of the liquid volume at the wettability-contrast line is greater than 90°, i.e., when there is a distinct liquid bulge and the cross-section of the liquid volume resembles Fig. 4a. In this configuration, the net capillary force has a lengthwise component that propels the liquid volume in the forward direction. However, when the bulge has disappeared (cross-section resembles Fig. 4b), the net capillary force reverses its direction and retards the spreading of the droplet, causing the fluid to slow down. The liquid volume still moves forward, decelerating along the course due to viscous drag, and finally there is an instant when the liquid spreads at an extremely slow rate, almost coming to a halt (Fig. 3g). This near-stationary liquid volume still has a local curvature, and acts as a source for the thin film that creeps sluggishly towards the wider end of the track (Fig. 3h).

Figure 5 shows time-lapse images of a 50% (by mass) glycerol in water droplet spreading on an identical track. The modes of spreading are identical to those of a water droplet (Fig. 3), with the only difference being the time instants at which the aforementioned salient spreading features are observed. The time stamps in Fig. 5 clearly indicate that the glycerol solution spreads much slower than water. This is expected, as the viscosity of this solution is approximately 5 times that of water; Table 1. The viscous force opposes the capillary force, resulting in a much weaker net driving force acting on the liquid volume. The magnitude of the capillary force is directly proportional to the liquid surface tension[4] which, as per Table 1, decreases slightly due to the addition of glycerol in the water. However, this reduction in surface tension is minimal (Table 1). Weakening of the net driving force results in the droplet to spread much slower; even at the end of the recording window in this case, the liquid front has not reached the end of the track (Fig. 5h). Supplementary Videos 1 and 2 show high-speed videos of the respective spreading events of Figs 3 and 5, while Supplementary Video 3 shows a simultaneous high-speed top and side view video corresponding to Fig. 3.

Dynamics of spreading

Image processing of the high-speed videos correlates quantitatively the liquid front position (x) with time (t). This variation is plotted in Fig. 6 for different mass fractions (C_m) of glycerol/water solutions. All the curves show similar trend, where the front position initially increases rapidly with time, and then progresses much slower. The trend observed for increasing glycerol mass fractions is also expected. A water droplet ($C_m = 0$) has the lowest viscosity among all fluids tested, and reaches the end of the track in 1.2 s. On the other hand, a 50 wt. % droplet does not reach the end of

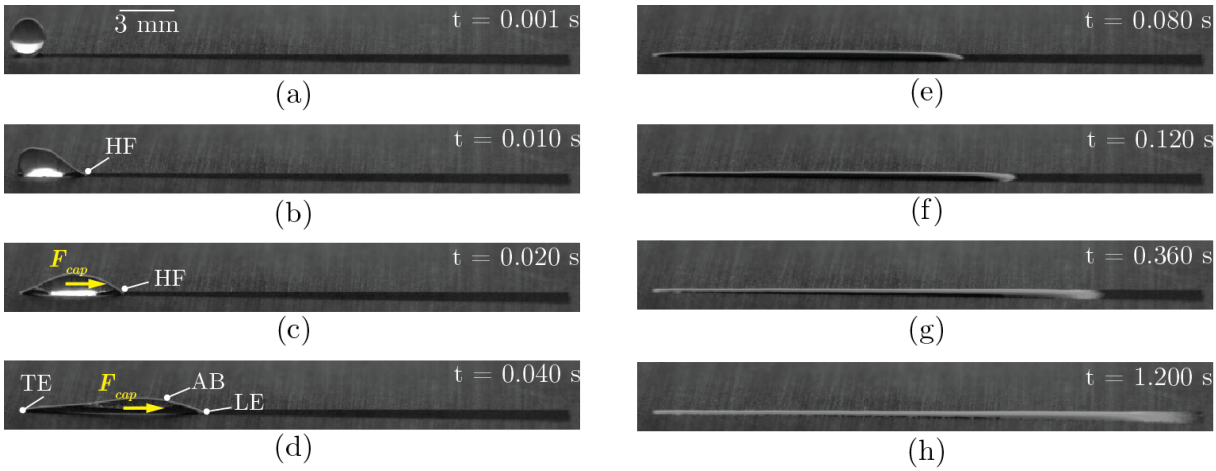

Figure 3: Time-lapse images of water droplet spreading on a wettability-confined wedge-shaped track: (a) instant of droplet touching the narrow end of the track (t = 0.001 s); (b) bulge volume stationary, while hemiwicking front (HF) advances (t = 0.010 s); (c, d, e) both bulge and liquid front move together, with the advancing bulge (AB) gradually decreasing in height (t = 0.020, 0.040, 0.080 s); (f) bulge has disappeared and entire liquid volume moves as a rivulet (t = 0.120 s); (g) bulk liquid has become almost stationary and acts as a source for liquid spreading on the superhydrophilic surface at a much slower rate (t = 0.360 s); (h) liquid front reaches the end of the track (t = 1.200 s)

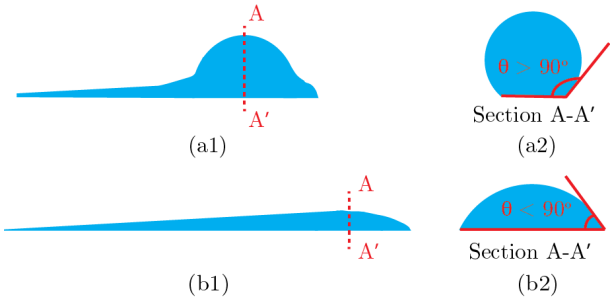

Figure 4: (a1) Generic liquid volume shape (side view) when bulge exists; (a2) cross-section of liquid volume (at section A-A′) when bulge exists, contact angle (θ) at wettability-contrast line greater than 90°; (b1) generic liquid volume shape when bulge has disappeared; (b2) cross-section of liquid volume (at section A-A′) when bulge has disappeared, contact angle (θ) at wettability-contrast line smaller than 90°

the track even after 3.87 s. The similarity in the trends of the curves for the fluids with different viscosities suggests that an appropriate non-dimensionalization of the key parameters related to the directional spreading would lead to a single curve for all the fluids tested, revealing the underlying physics of the problem and allowing predictions of spreading behavior for other fluids without prior experimental testing.

The dimensionless liquid front location, X, was defined as x/L, where L denotes the total length of the respective track; the dimensionless time, T, was defined as $\gamma t/\mu L$, where γ and μ denote the fluid surface tension and viscosity, respectively. The variation of X with T is plotted in Fig. 7 for all the working fluids considered in this work. It is observed that the nondimensional displacement-time curves for all the fluids collapse upon each other. Three distinct regimes of spreading are observed, which have been marked in Fig. 7 as I, II, and III, respectively. Regime I corresponds to the time period when the liquid bulge has not yet picked up noticeable velocity (due to its inertia), and only a thin film advances from it (Figs. 3b and 5b). Liquid transport in this regime takes place primarily by hemiwicking through the

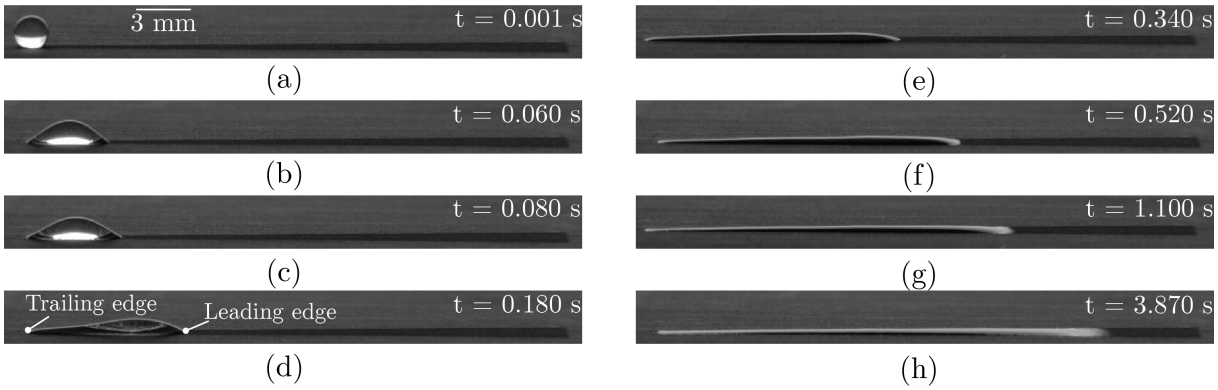

Figure 5: Time-lapse images of 50 wt. % glycerol in water droplet spreading on a wettability-confined wedge-shaped track: (a) instant of droplet touching the narrow end of the track (t = 0.001 s); (b) bulge volume stationary while hemiwicking front advances (t = 0.060 s); (c, d, e) both bulge and liquid front move together, with the bulge gradually decreasing in height (t = 0.080, 0.180, 0.340 s); (f) bulge has disappeared and entire liquid volume moves as a rivulet (t = 0.520 s); (g) bulk liquid has become almost stationary and acts as a source for liquid spreading on superhydrophilic surface at a much slower rate (t = 1.100 s); (h) liquid front still has not reached the end of the track at t = 3.870 s.

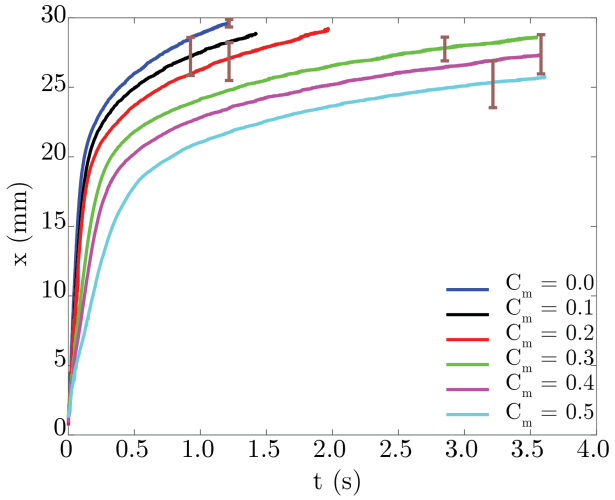

Figure 6: Liquid front location (x) at different time instants (t); C_m indicates the mass fraction of glycerol in water solution; error bars indicate the maximum error for each curve.

crevices of the rough, superhydrophilic track. The flow in this mode is mainly influenced by two forces: the capillary-pull through the crevices (which may be assumed analogous to a bundle of hydrophilic microchannels[19]) on the rough track, and the viscous force opposing the flow. In the early spreading regime of viscous droplets on unbounded substrates, researchers[62,63] have shown that the spreading distance varies with $t^{1/2}$, as in the Washburn spreading law.[64] The same scaling relationship was obtained by Schutzius et al.[19] for unidirectional droplet spreading on rectangular surface tension confined tracks. The lower left inset in Fig. 7 presents the variation of X with $T^{1/2}$ in Regime I, which shows that the data points for all fluids follow, approximately, a straight line (dashed line). The departures from the straight-line behavior is attributed to the observed oscillations in the liquid during the early moments of spreading, after the droplet has just touched the substrate, following dispension from the nozzle (Supplementary Videos 1 and 2). When the spreading distance, x, is much larger (by more than two orders of magnitude in the present case) than the average pore diameter of the roughness structures on the surface, d_{pore}, the velocity u of the liquid front may be

approximated as a Poiseuille flow

$$u \sim \frac{d_{pore}^2}{\mu}\frac{\Delta p}{x} \tag{1}$$

Here Δp is the capillary pressure difference driving the flow. The mean curvature of the liquid meniscus at the crevices of the surface microstructures at the wetting front is $\sim 1/d_{pore}$, which leads to

$$\Delta p \sim \frac{\gamma}{d_{pore}} \tag{2}$$

Rewriting u as x/t, Eq. 1 becomes

$$\frac{x}{t} \sim \frac{\gamma}{\mu}\frac{d_{pore}}{x} \tag{3}$$

which is analogous to the Washburn relationship,

$$x \sim \left(\frac{\gamma}{\mu}\right)^{1/2} t^{1/2} \tag{4}$$

The lower left inset of Fig. 7 thus shows that the spreading front in Regime I indeed exhibits a Washburn-type scaling, indicating that the liquid spreading is primarily attributed to hemiwicking on the textured superhydrophilic surface. Regime I commences from the moment the droplet touches the superhydrophilic track and lasts up to the point where the liquid bulge overcomes its inertia and starts moving.

Liquid spreading in the second regime is governed by a balance between the capillary force (arising out of the shape of the liquid meniscus of the traveling liquid bulge) that propels the liquid forward and the viscous force resisting its motion. The axial component of the capillary force acting on the liquid bulge is estimated by

$$F_{cap} \sim \frac{dp}{dx} A_{cs} x \tag{5}$$

where dp/dx denotes the Laplace pressure gradient along the axial direction and A_{cs} denotes the cross-sectional area of the bulge upon which the Laplace pressure acts. The Laplace pressure gradient can be expressed as[4]

$$\frac{dp}{dx} \sim 2\gamma sin\theta_{avg}\frac{1}{\delta^2}\alpha \tag{6}$$

where θ_{avg} is the average contact angle of the liquid along the wettability-contrast line over the length of the bulge, and δ denotes the local track width. As the liquid volume spreads, θ_{avg} changes from obtuse to acute, causing $sin\theta_{avg}$ to reverse its sign. Moreover, the diverging nature of the track means that δ increases as the liquid spreads, thus decreasing the magnitude of the driving pressure gradient. Hence the spreading liquid volume eventually slows down. Assuming the cross-section of the bulge to be a sector of a circle, $A_{cs} \sim \delta^2$. Therefore, for a fixed value of α, $F_{cap} \sim \gamma x$. The viscous resistance at the base of the moving bulge, on the other hand, can be approximated as

$$F_{visc} \sim \mu\frac{u}{h}A_{base} \tag{7}$$

where u is the linear velocity of the liquid volume, h the height of the bulge, and A_{base} represents the basal (footprint) area of the bulge volume. For a bulge cross-section that is a sector of a circle, $h \sim \delta$; and a trapezoidal approximation of the footprint of the bulge leads to $A_{base} \sim \frac{1}{2}x\delta$. Therefore, the viscous force can be written as

$$F_{visc} \sim \mu\frac{u}{h}x\delta \sim \mu\frac{x^2}{t} \tag{8}$$

A balance between the two aforementioned forces yields

$$x \sim \frac{\gamma}{\mu}t \ , \tag{9}$$

a linear dependence of the front position on time. The same linear scaling ($X \sim T$) has been observed experimentally as well, as shown in Fig. 7 for Regime II.

The third regime corresponds to the instant when the bulk liquid volume comes nearly to rest and a thin liquid film creeps on the superhydrophilic substrate (Figs. 3g and 5g). The dynamics in this regime are governed by the energy dissipation during spreading. De Gennes,[51] in his seminal paper on spreading of fluids, mentions that this energy dissipation is primarily attributed to three components – viscous dissipation in the bulk of the droplet, dissipation at the contact line,[65] and dissipation at the spreading precursor film.[12]

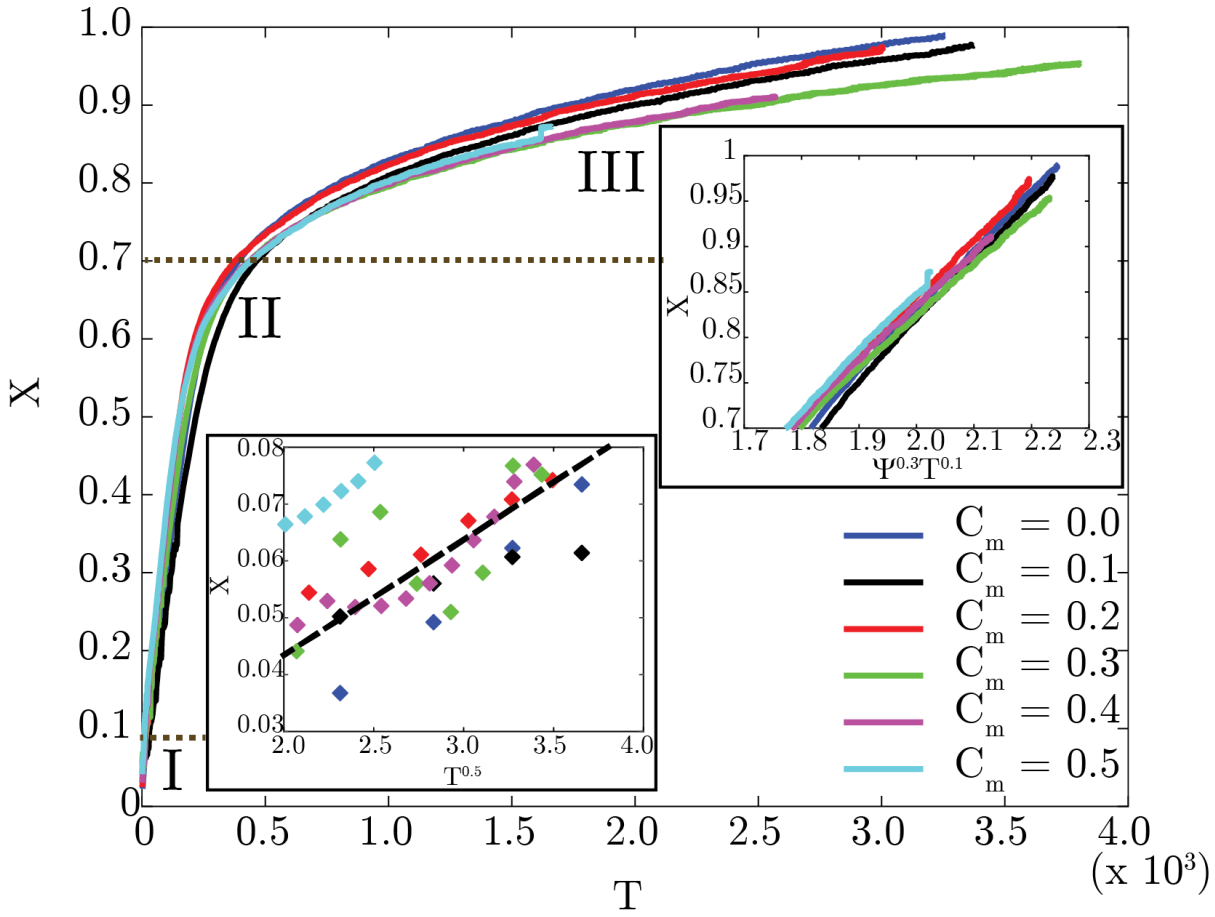

Figure 7: Dimensionless front location (X) plotted against dimensionless time (T); three distinct regimes are identified and marked as I, II, and III; the inset at lower left shows Regime I plotted against the Washburn scale of droplet spreading; the inset at top right shows Regime III plotted against the density augmented-Tanner spreading scale. The dashed line in the lower left inset shows the straight line that the datapoints approximately follow. The location of the transition from one regime to the next has been determined by plotting X against T in the log-log scale, as shown in Fig. S2 of the Supplementary Information.

The viscous dissipation in the bulk droplet is caused by a 'rolling motion' observed on the liquid surface, akin to a caterpillar track, as the droplet spreads.[66] By virtue of this rolling motion, packets of liquid that are on the free surface of the liquid volume eventually end up at the vicinity of the solid surface. On unbounded substrates, dissipation-governed spreading follows the well-known Tanner law,[67] where the spreading distance scales as $t^{1/10}$. For such a flow, following the lubrication approximation, the equation for the liquid-front velocity (assuming a Poiseuille flow) is given by

$$u \sim \frac{h^2}{\mu}\frac{\Delta p}{x} \tag{10}$$

where h denotes the height of the spreading liquid. For $h \ll x$, the mean curvature of the spreading front is $\sim h/x^2$,[68] and the pressure drop is given by

$$\Delta p \sim \gamma \frac{h}{x^2} \tag{11}$$

Therefore, the spreading velocity can be rewritten as

$$u = \frac{x}{t} \sim \frac{\gamma}{\mu}\frac{h^3}{x^3} \tag{12}$$

In Regime III, h is not constant but varies with x. Instead, the spreading volume, Ω, is constant. Considering the spreading liquid volume to be part of a trapezoidal prism, we deduce from volume conservation,

$$\Omega \sim hx\delta \tag{13}$$

For small α, $\delta \sim \alpha x$, which leads to $\Omega \sim \alpha h x^2$, which further yields

$$h \sim \frac{\Omega}{\alpha x^2} \tag{14}$$

However, for tests with different fluids, Ω is not constant, as the pendant droplet size changes with fluid properties. Since the mass of the dispensed droplet is governed by a balance between gravity (that sheds the droplet) and surface tension (that restrains the drop at the needle tip),[69,70] one may account for the effect of density variation on the dispensed volume using

$$\Omega \sim \Omega_0 \frac{\rho_0}{\rho} \tag{15}$$

where ρ denotes the density of the fluid, and the subscript 0 corresponds to pure water. The effect of surface tension is ignored in Eq. 15, since that property did not differ noticeably between the fluid samples (Table 1), as compared to the density. Thus,

$$\begin{aligned} \frac{x}{t} &\sim \frac{\gamma}{\mu}\frac{1}{x^3}\Omega_0^3\left(\frac{\rho_0^3}{\rho^3}\right)\frac{1}{\alpha^3 x^6} \\ &\sim \frac{\gamma}{\mu}\frac{\Omega_0^3}{\alpha^3}\Psi^3\frac{1}{x^9} \end{aligned} \tag{16}$$

where Ψ denotes the ratio of ρ_0 and ρ. This, in turn, for constant wedge angle yields the spreading law

$$x \sim \Psi^{3/10}\left(\frac{\gamma}{\mu}\right)^{1/10} t^{1/10} \tag{17}$$

This scaling relationship resembles Tanner's spreading law,[67] with a weak density dependence. The upper right inset in Fig. 7 presents the variation of X with $\Psi^{3/10}T^{1/10}$ for all cases considered herein. All curves overlap and follow a straight line, which suggests that the spreading front in Regime III adheres to the $X \sim \Psi^{3/10}T^{1/10}$ scaling law – a density-augmented Tanner spreading law.

Although the above three spreading laws were validated over a five-fold range of fluid viscosities and narrower ranges of surface tension and fluid densities, the scaling expressions include all these effects as well as track angle. Thus, in principle, one could use the present laws to predict spreading behavior of other liquids on tracks of different contact angles. Such predictions apply to many applications that rely on liquid microdroplet manipulation on open surfaces.

Conclusions

The present study investigates mm-sized droplet spreading on diverging, wettability-confined tracks, and highlights the differences

between the traditional spreading on unconfined substrates or parallel tracks and the pumpless rapid transport observed on diverging tracks. A superhydrophilic trapezoidal or wedge-shaped track laid on a superhydrophobic background was used to study the droplet spreading behavior. Water and aqueous solutions of glycerol (mass fractions 0.1 – 0.5) were used as the working fluids to mimic biofluids. High-speed imaging showed that the droplet spreading morphologies are similar for the range of viscosities tested, the difference being that the time required to reach a particular spreading shape increased with increasing viscosity. The droplet initially remained stationary in the form of a liquid bulge, with a thin precursor film of liquid hemiwicking through the roughness structures of the superhydrophilic track terrain. After some time, both the liquid front and the liquid bulge moved, with the bulge decreasing in height as it spread until the point where the entire liquid volume spread as a slender rivulet. Finally, the bulk of the liquid volume became stationary, but a thin sluggish liquid front spread across the rest of the superhydrophilic track.

The variation of the liquid front position with time followed the changes in the liquid-spreading morphologies and spreading speeds. The fluid with the lowest viscosity (water) was found to be spreading fastest, and the one with the highest viscosity (50% glycerol in water) spreading the slowest, with all the intermediate fluids having spreading characteristics in between these two extremes in order of ascending viscosity.

A dimensionless front position (X) and a dimensionless time (T) were introduced, and all spreading curves were found to collapse upon each other. Three regimes identified by observing the spreading shapes were apparent in the X vs. T plot. In the first regime, the directional transport resembled the early-stage spreading of unconfined viscous droplets through hemiwicking, and the spreading front was observed to follow the Washburn law ($X \sim T^{1/2}$). The second regime corresponded to a balance between the capillary force driving the liquid bulge and the viscous resistive force, where a linear scaling relationship ($X \sim T$) was observed. Finally, in the third and final spreading regime, the dissipation at the contact line dictated the spreading behavior, and the front advanced following a density-augmented Tanner law ($X \sim \Psi^{3/10}T^{1/10}$, where Ψ is a density ratio). Such multiscale spreading has also been observed by other researchers[62,63,68] for spreading of droplets on unconfined substrates; this, however, is the first work that identifies multliple regimes of spreading when a droplet spreads on a diverging, wettability-confined track.

The principal objective of the present work was to find the scaling laws for the spreading behavior of liquids on wettability-confined, diverging tracks, and the results indicate that this objective was successfully achieved. The viscosity of the liquids was changed in a parametric fashion (over a factor of five) in order to arrive at those scaling laws. The same could have been achieved with any other fluid property variation, and the results obtained thereafter would still have fallen on the curves shown in Fig. 7. Despite the fact that the present study concentrated on aqueous liquids, the approach applies to non-aqueous liquids as well. In other words, if one created similar patterns for oils (oleophilic tracks on oleophobic terrain), one would expect the present scaling laws to hold there as well.

Although the present experiments featured wettability-confined tracks with fixed length and a particular diverging angle, the spreading regimes and scaling arguments extend to tracks of other lengths (L) in the cm range, as L explicitly appeared in the dimensionless variables (X and T). Moreover, the wedge angle (α) was implicitly considered while deriving the scaling arguments, thus the present results should apply to other angles up to $\sim 10^\circ$ or even larger.

The present study described the directional spreading behavior of viscous liquid droplets on wettability-patterned diverging tracks, and is the first of its kind. Scaling laws of the advancing liquid front with time were identified and explained. These tracks have potential applications in point-of-care diagnostic devices, liquid mixing, and transport of oils and organic solvents – applications where the working fluid

may have a diverse range of fluid properties. In such cases, it is important to know how far and how fast the fluid will spread on a particular geometry. Such information should facilitate design decisions and improvement of the performance of the device itself.

Supporting Information

Supplementary Information. Scanning electron micrograph of laser-ablated region (superhydrophilic) of a typical aluminum sample; average dimensionless front location (X) plotted against dimensionless time (T) in log-log scale in order to identify the transition from one regime to the next.

Supplementary Video 1. Spreading of water droplet on wettability-confined wedge-shaped track.

Supplementary Video 2. Spreading of a droplet of 50% aqueous solution of glycerol on wettability-confined wedge-shaped track.

Supplementary Video 3. Simultaneous top and side view of water droplet spreading on wettability-confined wedge-shaped track.

Acknowledgement

The authors are grateful to Kimberly-Clark Corporation for their generous financial support during the course of this study. The Laser Marking System, Scanning Electron Microscope, and the Optical Profilometer equipments of the Nanotechnology Core Facility in UIC were used for sample fabrication and characterization, with the valuable assistance of Jared M. Morrissette and Theodore P. Koukoravas of the UIC Micro/Nanoscale Fluid Transport Laboratory. The authors would also like to thank David Mecha of the Engineering Machine Shop in UIC for assistance with sample fabrication. Finally, the authors would like to thank Aritra Ghosh of the UIC Micro/Nanoscale Fluid Transport Laboratory for providing resources on the state-of-the-art in open-surface microfluidics.

References

(1) Kaigala, G. V.; Lovchik, R. D.; Delamarche, E. Microfluidics in the "open space" for performing localized chemistry on biological interfaces. *Angew. Chem. Int. Ed.* **2012**, *51*, 11224–11240.

(2) Hourtane, V.; Bodiguel, H.; Colin, A. Dense bubble traffic in microfluidic loops: selection rules and clogging. *Phys. Rev. E* **2016**, *93*, 032607.

(3) Cong, H.; Xu, X.; Yu, B.; Liu, H.; Yuan, H. Fabrication of anti-protein-fouling poly(ethylene glycol) microfluidic chip electrophoresis by sandwich photolithography. *Biomicrofluidics* **2016**, *10*, 044106.

(4) Ghosh, A.; Ganguly, R.; Schutzius, T. M.; Megaridis, C. M. Wettability patterning for high-rate, pumpless fluid transport on open, non-planar microfluidic platforms. *Lab Chip* **2014**, *14*, 1538–1550.

(5) Zhao, Y.; Wang, H.; Zhou, H.; Lin, T. Directional fluid transport in thin porous materials and its functional applications. *Small* **2017**, *13*, 1601070.

(6) Smith, J. D.; Dhiman, R.; Anand, S.; Reza-Garduno, E.; Cohen, R. E.; McKinley, G. H.; Varanasi, K. K. Droplet mobility on lubricant-impregnated surfaces. *Soft Matter* **2013**, *9*, 1772–1780.

(7) Choi, K.; Ng, A. H. C.; Fobel, R.; Wheeler, A. R. Digital microfluidics. *Annu. Rev. Anal. Chem.* **2012**, *5*, 413–440.

(8) Nelson, W. C.; Kim, C. J. Droplet actuation by electrowetting-on-dielectric (EWOD): a review. *J. Adhes. Sci. Technol.* **2012**, *26*, 1747–1771.

(9) Park, S. Y.; Teitell, M. A.; Chiou, E. P. Y. Single-sided continuous optoelectrowetting (SCOEW) for droplet manipulation with light patterns. *Lab Chip* **2010**, *10*, 1655–1661.

(10) Long, Z.; Shetty, A. M.; Solomon, M. J.; Larson, R. G. Fundamentals of magnet-actuated droplet manipulation on an open hydrophobic surface. *Lab Chip* **2009**, *9*, 1567–1575.

(11) Foresti, D.; Nabavi, M.; Klingauf, M.; Ferrari, A.; Poulikakos, D. Acoustophoretic contactless transport and handling of matter in air. *Proc. Natl. Acad. Sci.* **2013**, *110*, 12549–12554.

(12) de Gennes, P.-G.; Brochard-Wyart, F.; Quéré, D. *Capillarity and Wetting Phenomena: Drops, Bubbles, Pearls, Waves*; Springer-Verlag New York Inc., 2004.

(13) Greenspan, H. P. On the motion of a small viscous droplet that wets a surface. *J. Fluid Mech.* **1978**, *84*, 125–143.

(14) Gau, H.; Herminghaus, S.; Lenz, P.; Lipowsky, R. Liquid morphologies on structured surfaces: from microchannels to microchips. *Science* **1999**, *283*, 46–49.

(15) Feng, X.; Jiang, L. Design and creation of superwetting/antiwetting surfaces. *Adv. Mater.* **2006**, *18*, 3063–3078.

(16) Balu, B.; Berry, A. D.; Hess, D. W.; Breedveld, V. Patterning of superhydrophobic paper to control the mobility of micro-liter drops for two-dimensional lab-on-paper applications. *Lab Chip* **2009**, *9*, 3066–3075.

(17) Seo, J.; Lee, S.; Lee, J.; Lee, T. Guided transport of water droplets on superhydrophobic-hydrophilic patterned Si nanowires. *ACS Appl. Mater. Interfaces* **2011**, *3*, 4722–4729.

(18) Mertaniemi, H.; Jokinen, V.; Sainiemi, L.; Franssila, S.; Marmur, A.; Ikkala, O.; Ras, R. H. A. Superhydrophobic tracks for low-friction, guided transport of water droplets. *Adv. Mater.* **2011**, *23*, 2911–2914.

(19) Schutzius, T. M.; Elsharkawy, M.; Tiwari, M. K.; Megaridis, C. M. Surface tension confined (STC) tracks for capillary-driven transport of low surface tension liquids. *Lab Chip* **2012**, *12*, 5237–5242.

(20) Elsharkawy, M.; Schutzius, T. M.; Megaridis, C. M. Inkjet patterned superhydrophobic paper for open-air surface microfluidic devices. *Lab Chip* **2014**, *14*, 1168–1175.

(21) Yamada, Y.; Ikuta, T.; Nishiyama, T.; Takahashi, K.; Takata, Y. Droplet nucleation on a well-defined hydrophilic-hydrophobic surface of 10 nm order resolution. *Langmuir* **2014**, *30*, 14532–14537.

(22) Piorek, B. D.; Lee, S. J.; Santiago, J. G.; Moskovits, M.; Banerjee, S.; Meinhart, C. D. Free-surface microfluidic control of surface-enhanced Raman spectroscopy for the optimized detection of air molecules. *Proc. Natl. Acad. Sci.* **2007**, *104*, 18898–18901.

(23) Seo, J.; Lee, S. K.; Lee, J.; Lee, J. S.; Kwon, H.; Cho, S. W.; Ahn, J. H.; Lee, T. Path-programmable water droplet manipulations on an adhesion controlled superhydrophobic surface. *Sci. Rep.* **2015**, *5*, 12326.

(24) Kang, H.; Heo, Y. J.; Kim, D. J.; Kim, J. H.; jeon, T. Y.; Cho, S.; So, H. M.; Chang, W. S.; Kim, S. H. Droplet-guiding superhydrophobic arrays of plasmonic microposts for molecular concentration and detection. *ACS Appl. Mater. Interfaces* **2017**,

(25) Martinez, A. W.; Phillips, S. T.; Whitesides, G. M.; Carrilho, E. Diagnostics for the developing world: microfluidic paper-based analytical devices. *Anal. Chem.* **2010**, *82*, 3–10.

(26) Choudhary, T.; Rajamanickam, G. P.; Dendukuri, D. Woven electrochemical fabric-based test sensors (WEFTS): a new class of multiplexed electrochemical sensors. *Lab Chip* **2015**, *15*, 2064–2072.

(27) Darhuber, A. A.; Troian, S. M. Principles of microfluidic actuation by modulation of surface stresses. *Annu. Rev. Fluid Mech.* **2005**, *37*, 425–455.

(28) Bliznyuk, O.; Jansen, H. P.; Kooij, E. S.; Zandvliet, H. J. W.; Poelsema, B. Smart design of stripe-patterned gradient surfaces to control droplet motion. *Langmuir* **2011**, *27*, 11238–11245.

(29) Lv, C.; Hao, P. Driving droplet by scale effect on microstructured hydrophobic surfaces. *Langmuir* **2012**, *2012*, 16958–16965.

(30) Sommers, A. D.; Brest, T. J.; Eid, K. F. Topography-based surface tension gradients to facilitate water droplet movement on laser-etched copper substrates. *Langmuir* **2013**, *29*, 12043–12050.

(31) Chaudhury, M. K.; Whitesides, G. M. How to make water run uphill. *Science* **1992**, *256*, 1539–1541.

(32) Dos Santos, F. D.; Ondarçuhu, T. Free-running droplets. *Phys. Rev. Lett.* **1995**, *75*, 2972–2975.

(33) Cira, N. J.; Benusiglio, A.; Prakash, M. Vapor-mediated sensing and motility in two-component droplets. *Nature* **2015**, *519*, 446–450.

(34) Chakraborty, M.; Ghosh, U. U.; Chakraborty, S.; DasGupta, S. Thermally enhanced self-propelled droplet motion on gradient surfaces. *RSC Adv.* **2015**, *5*, 45266–45275.

(35) Ichimura, K.; Oh, S. K.; Nakagawa, M. Light-driven motion of liquids on a photoresponsive surface. *Science* **2000**, *288*, 1624–1626.

(36) Zhao, Y.; Liu, F.; Chen, C. H. Thermocapillary actuation of binary drops on solid surfaces. *Appl. Phys. Lett.* **2011**, *99*, 104101.

(37) Li, Y.; He, L.; Zhang, X.; Zhang, N.; Tian, D. External-field-induced gradient wetting for controllable liquid transport: from movement on the surface to penetration into the surface. *Adv. Mater.* **2017**,

(38) Zhang, J.; Han, Y. Shape-gradient composite surfaces: water droplets move uphill. *Langmuir* **2007**, *23*, 6136–6141.

(39) Hirai, Y.; Mayama, H.; Matsuo, Y.; Shimomura, M. Uphill water transport on a wettability-patterned surface: experimental and theoretical results. *ACS Appl. Mater. Interfaces* **2017**, *9*, 15814–15821.

(40) Lorenceau, E.; Quéré, D. Drops on a conical wire. *J. Fluid Mech.* **2004**, *510*, 29–45.

(41) Khoo, H. S.; Tseng, F.-G. Spontaneous high-speed transport of subnanoliter water droplet on gradient nanotextured surfaces. *Appl. Phys. Lett.* **2009**, *95*, 063108.

(42) Alheshibri, M. H.; Rogers, N. G.; Sommers, A. D.; Eid, K. F. Spontaneous movement of water droplets on patterned Cu and Al surfaces with wedge-shaped gradients. *Appl. Phys. Lett.* **2013**, *102*, 174103.

(43) Nakajima, A.; Nakagawa, Y.; Furuta, T.; Sakai, M.; Isobe, T.; Matsushita, S. Sliding of water droplets on smooth hydrophobic silane coatings with regular triangle hydrophilic regions. *Langmuir* **2013**, *29*, 9269–9275.

(44) Morrissette, J. M.; Mahapatra, P. S.; Ghosh, A.; Ganguly, R.; Megaridis, C. M. Rapid, self-driven liquid mixing on open-surface microfluidic platforms. *Sci. Rep.* **2017**, *7*, 1800.

(45) Ghosh, A.; Beaini, S.; Zhang, B. J.; Ganguly, R.; Megaridis, C. M. Enhancing dropwise condensation through bioinspired wettability patterning. *Langmuir* **2014**, *30*, 13103–13115.

(46) Mahapatra, P. S.; Ghosh, A.; Ganguly, R.; Megaridis, C. M. Key design and operating parameters for enhancing dropwise

condensation through wettability patterning. *Int. J. Heat Mass Transfer* **2016**, *92*, 877–883.

(47) Tan, X.; Zhu, Y.; Shi, T.; Tang, Z.; Liao, G. Patterned gradient surface for spontaneous droplet transportation and water collection: simulation and experiment. *J. Micromech. Microeng.* **2016**, *26*, 115009.

(48) Koukoravas, T. P.; Ghosh, A.; Mahapatra, P. S.; Ganguly, R.; Megaridis, C. M. Spatially-selective cooling by liquid jet impinging orthogonally on a wettability-patterned surface. *Int. J. Heat Mass Transfer* **2016**, *95*, 142–152.

(49) Huang, S.; Song, J.; Lu, Y.; Chen, F.; Zheng, H.; Yang, X.; Liu, X.; Sun, J.; Carmalt, C. J.; Parkin, I. P.; Xu, W. Underwater spontaneous pumpless transportation of nonpolar organic liquids on extreme wettability patterns. *ACS Appl. Mater. Interfaces* **2016**, *8*, 2942–2949.

(50) Ody, T.; Panth, M.; Sommers, A. D.; Eid, K. F. Controlling the motion of ferrofluid droplets using surface tension gradients and magnetoviscous pinning. *Langmuir* **2016**, *32*, 6967–6976.

(51) de Gennes, P. G. Wetting: statics and dynamics. *Rev. Mod. Phys.* **1985**, *57*, 827–863.

(52) Šikalo, Š.; Wilhelm, H.-D.; Roisman, I. V.; Jakirlić, S.; Tropea, C. Dynamic contact angle of spreading droplets: experiments and simulations. *Phys. Fluids.* **2005**, *17*, 062103.

(53) Seveno, D.; Vaillant, A.; Rioboo, R.; Adão, A.; Conti, J.; de Coninck, J. Dynamics of wetting revisited. *Langmuir* **2009**, *25*, 13034–13044.

(54) Bonn, D.; Eggers, J.; Indekeu, J.; Meunier, J.; Rolley, E. Wetting and spreading. *Rev. Mod. Phys.* **2009**, *81*, 739–805.

(55) Vedder, W.; Vermilyea, D. A. Aluminum + water reaction. *Trans. Faraday Soc.* **1969**, *65*, 561–584.

(56) Zhijia, Y.; Yuefei, Y.; Yangfeng, L.; Shanpeng, S.; Subin, H.; Xiuyan, H. Preparation and characterization of superhydrophobic surfaces on aluminum and stainless steel substrates. *Surf. Rev. Lett.* **2010**, *17*, 375–381.

(57) Yang, J.; Zhang, Z.; Xu, X.; Men, X.; Zhu, X.; Zhou, X. Superoleophobic textured aluminum surfaces. *New J. Chem.* **2011**, *35*, 2422–2426.

(58) Segur, J. B.; Oberstar, H. E. Viscosity of glycerol and its aqueous solutions. *Ind. Eng. Chem. Res.* **1951**, *43*, 2117–2120.

(59) Takamura, K.; Fischer, H.; Morrow, N. R. Physical properties of aqueous glycerol solutions. *J. Pet. Sci. Eng.* **2012**, *98-99*, 50–60.

(60) Quéré, D. Wetting and roughness. *Annu. Rev. Mater. Res.* **2008**, *38*, 71–99.

(61) Brinkmann, M.; Liposwky, R. Wetting morphologies on substrates with striped surface domains. *J. Appl. Phys.* **2002**, *92*, 4296–4306.

(62) Carlson, A.; Bellani, G.; Amberg, G. Universality in dynamic wetting dominated by contact-line friction. *Phys. Rev. E* **2012**, *85*, 045302 (R).

(63) Winkels, K. G.; Weijs, J. H.; Eddi, A.; Snoeijer, J. H. Initial spreading of low-viscosity drops on partially wetting surfaces. *Phys. Rev. E* **2012**, *85*, 055301 (R).

(64) Washburn, E. W. The dynamics of capillary flow. *Phys. Rev.* **1921**, *XVII*, 273–283.

(65) Carlson, A.; Bellani, G.; Amberg, G. Contact line dissipation in short-time dynamic wetting. *Europhys. Lett.* **2012**, *97*, 44004.

(66) de Rujiter, M. J.; De Coninck, J.; Oshanin, G. Droplet spreading: partial wetting regime revisited. *Langmuir* **1999**, *15*, 2209–2216.

(67) Tanner, L. H. The spreading of silicone oil drops on horizontal surfaces. *J. Phys. D.* **1979**, *12*, 1473–1484.

(68) Biance, A. L.; Clanet, C.; Quéré, D. First steps in the spreading of a liquid droplet. *Phys. Rev. E* **2004**, *69*, 016301.

(69) Day, R. F.; Hinch, E. J.; Lister, J. R. Self-similar capillary pinchoff of an inviscid fluid. *Phys. Rev. Lett.* **1998**, *80*, 704–707.

(70) Chen, A. U.; Notz, P. K.; Basaran, O. A. Computational and experimental analysis of pinch-off and scaling. *Phys. Rev. Lett.* **2002**, *88*, 174501.

Table of Contents Graphic